Nuclear Materials and Energy 27 (2021) 100965

Contents lists available at ScienceDirect

Nuclear Materials and Energy

journal homepage: www.elsevier.com/locate/nme

Experimental verification of ion impact angle distribution at divertor surfaces using micro-engineered targets on DiMES at DIII-D

S. Abe [a,*], C.H. Skinner [b], I. Bykov [c], Y.W. Yeh [d], A. Lasa [e], J. Coburn [f], D.L. Rudakov [c], C. J. Lasnier [g], H.Q. Wang [h], A.G. McLean [g], T. Abrams [h], B.E. Koel [a]

[a] Department of Chemical and Biological Engineering, Princeton University, Princeton, NJ 08540, USA
[b] Princeton Plasma Physics Laboratory, Princeton, NJ 08543, USA
[c] Center for Energy Research, University of California San Diego, CA 92093, USA
[d] Department of Physics and Astronomy, Rutgers, The State University of New Jersey, Piscataway, NJ 08854, USA
[e] University of Tennessee, Knoxville, TN 37996, USA
[f] ITER Organization, Route de Vinon-sur-Verdon, CS 90 046 Paul Lez Durance, France
[g] Lawrence Livermore National Laboratory, Livermore, CA 94550, USA
[h] General Atomics, San Diego, CA 92186, USA

ARTICLE INFO

Keywords:
Divertor
Sheath
Ion impact angle
Erosion
Deposition
DiMES
Plasma-material interaction
Surface analysis

ABSTRACT

We report the first detailed experimental verification of the polar deuterium ion impact angle distribution (IAD) on the DIII-D divertor surface in L-mode plasmas using micro-engineered trenches in samples mounted on the DiMES probe. These trenches were fabricated via focused ion beam (FIB) milling of a silicon surface partially coated with aluminum. The sample surfaces were exposed to eight repeat L-mode deuterium discharges (30 s total exposure time). The samples were examined by scanning electron microscopy (SEM), which revealed changes on the trench floor due to material deposition and evidence for shadowing of the incident deuterium ions by the trench walls. The areal distribution of carbon and aluminum deposition was measured by energy-dispersive X-ray spectroscopy (EDS). One-dimensional profiles of this deposition are in agreement with net erosion profiles calculated from a Monte Carlo micro-patterning and roughness (MPR) code for ion sputtering using as input the polar and azimuthal deuterium IADs reported previously (Chrobak et al., Nucl. Fusion 58, 106019 (2018)). The deposition profiles verified the characteristic shape of the polar IADs, which have a broad maximum from 79° to 86°, over the experimental range of 68°–83°, where 0° is the surface normal direction.

1. Introduction

The angle of incidence of ions at the surface of plasma facing components (PFCs) affects erosion, deposition, material migration, and PFC lifetime. Tokamak divertors employ a magnetic field incident at a shallow angle, <5°, to reduce the thermal power flux density on the PFC surface. However, the sputtering yield is highly sensitive to pitch angles below 10°–20° [1,2] and hence, the incident angle of ions impacting the PFC surface is important in estimating the PFC lifetime due to erosion. The trajectory of ions traveling near the surface is controlled by the Chodura or magnetic sheath [3–5]. The ions accelerate, gyrate, *B*-drift, and collide with other species until they impact the surface. The ion trajectory in the sheath has been modeled with equation of motion [3,6], fluid-Monte Carlo, and kinetic Particle-in-Cell calculations [7]. While these models have predicted the ion impact angle distributions (IADs), it has been challenging to capture the ion incident direction experimentally because the ion trajectory is strongly affected by the sub-millimeter scale sheath physics [3,6,7]. Confirming the predicted IADs by experiments not only verifies the ion trajectory model, but also verifies the sheath potential model employed in those calculations.

There have been a limited number of experimental studies of IADs. Model calculations of erosion and redeposition on rough surfaces were presented in ref. [6] and found to be in good agreement with the ASDEX-Upgrade data. Deposition patterns of Al, used as a tracer species, were studied for NSTX-U and DIII-D graphite samples using scanning Auger microscopy (SAM) and confocal microscopy [8]. The analysis revealed that the net deposition of Al was concentrated in micropore structures on the surfaces that were shadowed from the incoming ions in a

* Corresponding author.
E-mail address: shotaa@princeton.edu (S. Abe).

https://doi.org/10.1016/j.nme.2021.100965
Received 31 July 2020; Received in revised form 23 February 2021; Accepted 8 March 2021
Available online 16 March 2021

direction calculated by taking account of magnetic sheath. Coburn et al. [9] estimated the ion incident direction using micro trenches (10 × 10 × 4 μm deep) fabricated on SiC substrates that were exposed to a combination of L- and H-mode D plasmas via the DIII-D Divertor Material Evaluation System (DiMES) facility [10]. The ion impact pattern was calculated with a Monte Carlo micro-patterning and roughness (MPR) code based on the predicted IADs [7,11]. The calculated pattern showed good agreement with a damaged area on the trench floor that was measured by atomic force microscopy (AFM).

In this paper we report a verification of the polar D IAD, previously calculated for DIII-D L-mode D plasmas, by measuring net C and Al deposition profiles on the trench floor of a micro-engineered trench exposed to the plasmas by using DIII-D DiMES facility. The areal impurity deposition patterns for each element on the trench floor were analyzed after exposure. The net erosion profiles from the MPR code, which uses the calculated polar and azimuthal D IADs, are compared to the impurity deposition profiles.

2. Experiment

2.1. Samples design and fabrication

A schematic drawing of the Al-coated Si sample is shown with trench locations in Fig. 1(b). Micro-trenches 30 μm × 30 μm × 2 or 3 μm deep were created on a Si(1 1 1) single crystal (6 mm dia., 1.6 mm thick, 99.99% purity) surface using a focused ion beam (FIB) system (Helios NanoLab G3 UC DualBeam FIB) that used Ga ions at 30 keV to mill the surface. Only the 3-μm deep trenches will be used in this analysis. One-half of the Si surface was coated by 100 nm of Al using vapor deposition. The 3D geometry of the trenches was measured with a Bruker Dimension ICON3 atomic force microscope using a RTESP-300 tip (Bruker AFM Probes). Fig. 2 shows an AFM profile of a 3-μm deep trench. The side walls as measured by AFM have an apparent angle of 15-30° with respect to the surface normal due to the 15-25° side angles of the AFM tip. The scanning electron microscope (SEM) images (Fig. 3) taken from different angles can be used to determine that the trench has steeper walls with angles in the range 0-10° with respect to the surface normal. On the downstream sides, the upper half of the wall has an angled slope (~65°) to direct reflected ions away from the trench floor.

2.2. DIII-D L-mode plasma exposure

The sample analyzed for this report was located at the center of the DiMES probe (labeled as position '**S1**' in Fig. 1(a)). The DiMES probe head is made of graphite and has a diameter of 48 mm. The DiMES system is electrically grounded to the DIII-D vessel so that the samples

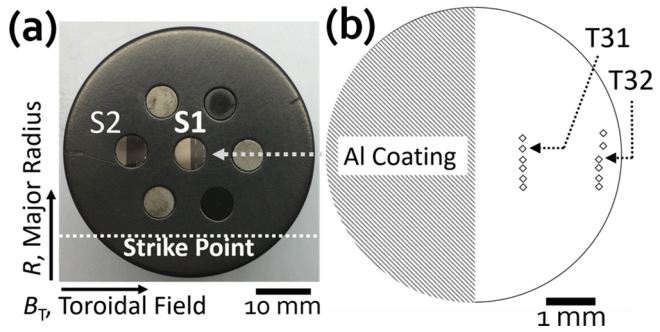

Fig. 1. (a) Optical image of the graphite DiMES sample holder. The sample at the center (labeled '**S1**') is the subject of this paper. (b) Schematic of sample '**S1**' with a 100-nm Al coating on the left. The locations of trenches are marked. The 30-μm trenches are expanded in this drawing by a scale factor of ×3 to make them more easily visible. The **T31** and **T32** trenches (3-μm deep) are indicated by dashed arrows. The trench profile is shown in Fig. 2.

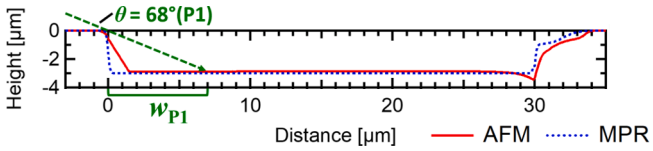

Fig. 2. Trench profiles measured by AFM (red solid line) and mathematically reproduced for the MPR calculation (blue dashed line). The shadowed range w_{P1} is indicated for discussions in Section 4. The polar angle **P1** is defined in Fig. 4.

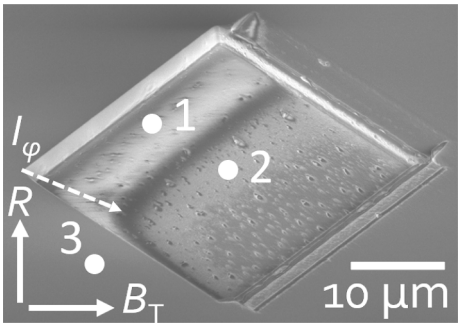

Fig. 3. SEM image of the engineered trench, **T31**, after plasma exposures. The SEM viewing angle is tilted by 45° from the surface normal. Solid and dashed arrows indicate the direction of the major radius R, the toroidal field B_T, and the peak azimuthal incident ion direction I_φ of D ions ($\varphi = -35°$, Section 3). The deposited material pattern can be seen as the bright area on the top left inside the trench. EDS spectra were taken at locations marked by **1**, **2**, and **3** (see Section 4.1).

are at the same potential as the divertor plates. The head center is located at a major radius of $R = 1.484$ m. The direction of the toroidal magnetic field B_T, and location of the outer strike point (OSP) (15 mm from the Si sample) is marked in Fig. 1(a). The OSP location could fluctuate by ±5 mm along the radial direction. This sample ('**S1**') was surrounded by five other tungsten discs covered by micro-carbon powders [12] and another silicon disc (labeled '**S2**' in Fig. 1(a)) that was also partially (40%) covered by Al. These samples were exposed to steady-state L-mode D plasmas for 30 s over eight discharges in DIII-D via the DiMES sample exposure facility. We note that the sample was exposed to three disruptions before and during those stable discharges. The peak incident flux from disruptions was measured as 10 times the average L-mode flux, but the duration was ~10 ms for each. Therefore, the cumulative heat/particle fluxes from these disruptions contributed just a few percent compared to those from the stable discharges. A surface Langmuir probe [13] located at $R = 1.50$ m recorded an electron temperature $T_e \sim 30$ eV, electron density $n_e \sim 0.7 \times 10^{13}$ cm^{-3}, and ion flux $I \sim 10^{18}$ cm^{-2}s^{-1} perpendicular to the divertor surface. Other important parameters were $B = 2.0$ T and the pitch angle $\alpha = 1.5°$ between the B direction and the sample surface. These parameters are averaged over a 0.5 s period during the stable flattop plasma current of ~3.5 s for each shot. The surface temperature T_{surf} of the samples was monitored with infrared (IR) thermography and did not exceed 250 °C. After plasma exposure, the sample was removed from the DiMES probe and mounted on gel in a plastic box (Gel-Box™, Gel-Pak®) for transportation to Princeton University and analysis at the PRISM Imaging and Analysis Center (IAC).

3. Computational model

The plasma conditions for the sample exposure were similar to "Case S-D" of ref. [3], which had $T_e \sim 30$ eV and $n_e \sim 1.2 \times 10^{13}$ cm^{-3}, and we adopt the D IADs calculated in ref. [3] in our modeling. Fig. 4 shows the polar (θ) IAD replotted from ref. [3]. A spherical coordinate system is

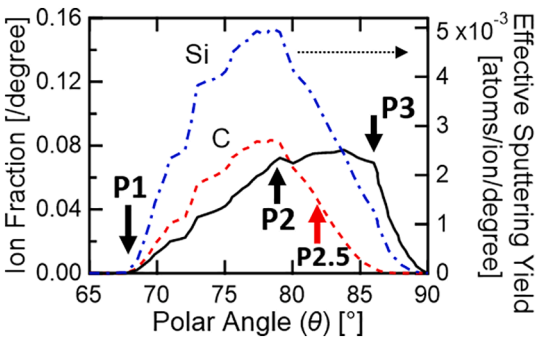

Fig. 4. The solid line represents the polar IAD replotted from "Case S-D" in ref. [3]. The left *y*-scale shows the fraction of ions incident per degree of a specific polar angle. The sputtering yield for C and Si at a specific polar angle was multiplied by the corresponding ion fraction at that angle to give the effective sputtering yield (defined in Section 3), and is shown for C and Si as red and blue dashed lines, respectively. Polar angles θ denoted by **P1**, **P2**, and **P3** correspond to 68°, 79°, and 86°, respectively. The **P2.5** angle, $\theta = 82°$ (C), is also defined in Section 4.

employed where the substrate surface normal is taken to be $\theta = 0°$ and the toroidal magnetic field B_T direction is taken to be the azimuthal angle $\varphi = 0°$. The IAD has no fractions from $\theta = 0°$ to the $\theta = 68°$ point marked as '**P1**'. The polar IAD reaches its maximal value at $\theta = 79°$ marked as '**P2**', which is maintained up to an angle of $\theta = 86°$ marked as '**P3**'. The azimuthal IAD profile shown in Fig. 6 of ref. [3] has a range of azimuthal angles $\varphi = -68°$ to $-28°$, with a sharp peak at $\varphi = -35°$ with respect to the toroidal magnetic field direction. We note that similar D IADs were calculated by a kinetic Particle-in-Cell method [7] for the shallow *B* incident angle ($\alpha = 85°$) although the plasma parameters used for the calculation ($T_e = 3$ eV, $n_e = 2 \times 10^{18}$ m^{-3}, and $B = 1.0$ T) were different from our experimental condition. The IADs calculated in ref. [7] peak at $\theta = 73°$ and $\varphi = -35°$, and are in good agreement with our IADs.

The Monte Carlo micro-patterning and roughness (MPR) code [9,14,15] models ion erosion, reflection, and migration due to ion bombardment on sculpted material surfaces. Herein it is used to calculate the net erosion yield on the trench floor surface. In the model, a flux of D ions with the polar and azimuthal IAD profiles introduced above, bombards C and Al surfaces comprising the trench with a model geometry close to the measured trench geometry (Fig. 2). The incident ion energy of D was taken to be $E_{impact} = 160$ eV. This value was estimated by summing the sheath potential drop scaled by the ion charge state and the average ion thermal energy using the relation $E_{impact} \sim 3Z_i kT_e + 2kT_i$ [16]. For ion temperatures T_i ranging from $T_i \sim T_e$ to $\sim 2T_e$, E_{impact} ranges from 150 to 210 eV. The energy dependence of sputtering and reflection rate coefficients was taken from the experimental fitting data, which are available in refs. [2] and [17]. The angular dependence for sputtering and reflection was taken from experimental data in these references. The sputtering and reflection rate coefficients were chosen from the values available in the databases that were nearest to 160 eV. For sputtering and reflection yield data for carbon, $E_{impact} = 140$ eV was used. $E_{impact} = 100$ eV was used for Si sputtering. Data for the angular dependence for sputtering and reflection on Al is not available for D bombardment, and so the data for Si was also used for Al. The incident angular dependence of D reflection on the Si surface was also not available and so He reflection data on Si for $E_{impact} = 200$ eV was used.

The sputtering yield for C and Si at a specific polar angle was multiplied by the corresponding ion fraction at that angle, and is plotted in Fig. 4 as the "effective sputtering yield" for C and Si as red and blue dashed lines, respectively. While the IAD continues at a high level up to an angle of $\theta = 86°$ ('**P3**'), both the C and Si effective sputtering yield peaks around $\theta = 77$–$79°$ ('**P2**') and then decreases at larger angles. For each calculation case, we used 2,880,000 ion impacts using the calculated IADs to produce random ion trajectories. For reflected and sputtered particles, the same cosine-like distribution was used given by

$$f(\theta_{out}) = g_1 \cos^{n1}(\theta_{out}) + g_2 \cos^{n2}(\theta_{out}) \quad (1)$$

where θ_{out} is the angle between the surface normal and direction of species emitted from the target surface. The coefficients $g_{1,2}$ and $n_{1,2}$ used in this calculation were assumed to be $g_1 = 1.5$, $g_2 = -1.0$, $n_1 = 0.1$ and $n_2 = 0.9$ [15]. Such distributions having $n_{1,2} < 1$ are defined as undercosine distributions [2] and have been reported previously for He bombardment for $E_{impact} = 225$ eV on C [18]. The calculated results are compared with experimental energy-dispersive X-ray spectroscopy (EDS) results in the next sections.

At an E_{impact}(D) = 150 eV ($\theta = 0°$), the chemical erosion yield is Y_{chem}(150 eV) = 0.0038 atoms/ion for T_{surf} = 400–500 K, while the calculated physical sputtering yield Y_{phys}(150 eV) = 0.020 according to the analytical equation given by in ref. [19]. Generally, a higher E_{impact} gives lower Y_{chem} and higher Y_{phys}, for example at $E_{impact} = 210$ eV, Y_{chem}(210 eV) = 0.00093 and Y_{phys}(210 eV) = 0.022. Thus, we assume that the erosion mechanism of C due to the D ion bombardment is dominated by physical sputtering and does not include chemical erosion. The chemical erosion yield of Si is about 10 times smaller than that for C [20], while the physical sputtering yield of Si has a similar value as that for C (as seen in Fig. 4). Thus, the erosion of Si is also dominated by its physical sputtering yield in this experiment. The physical sputtering yield of C due to the C bombardment is given by Y_{phys}(150 eV) = 0.12 [2], which is an order of magnitude higher than that for D. However, when we assume the incident ion C impurity is 1%, which is a typical value for the plasma parameters reported in ref. [3], the *total* physical sputtering of C due to the C bombardment is an order of magnitude smaller than that by D bombardment.

4. Results and discussion

4.1. EDS analysis and imaging

A SEM (Thermo Fisher Scientific., Verios 460 Extreme High-Resolution SEM) was used to image changes in morphology of the trenches due to plasma exposure. This same instrument was used for EDS analysis to reveal the deposited elements. An electron energy of 5.0 keV was utilized in order to obtain more near-surface chemical information, since the penetration depth of electrons at this energy in Si is 200 nm [21]. EDS peaks from C at 0.277 keV (C Kα), O at 0.525 keV (O Kα), Ga at 1.098 keV (Ga Lα), Al at 1.486 keV (Al Kα), and Si at 1.740 keV (Si Kα) were identified on the trench floors (labeled as locations **1** and **2** in Fig. 3) in this analysis. Figs. 3 and 5 (a) show SEM images of the 3-μm deep engineered trench '**T31**' (shown in Fig. 1(b)) after plasma exposures. The viewing angle of Figs. 3 and 5 are 45° and 0° from the surface normal, respectively, and the peak azimuthal incident ion direction ($\varphi = -35°$) of D ions is shown schematically as I_φ. The deposited material had a higher secondary electron emission coefficient, so its distribution pattern is apparent as the bright area on the top left of the trench floor in Fig. 3. The "corner" of the deposition pattern is consistent with I_φ. We note the presence of Ga microparticles on the trench floor, but not on the outside area; these features were apparent for all of the trenches. Since Ga ions were implanted in the Si surface during FIB milling, it seems likely that during the plasma exposures the surface temperature rose above the Ga melting point of 30 °C, and then the Ga condensed into solid particles when the surface cooled back to room temperature. Similar particle formation was reported in previous experiments using SiC substrates that also had microtrenches fabricated by Ga ion beams [9].

AZtec software (Oxford Instruments) was used to measure the elemental peak areas and generate 2D intensity data at a resolution of 0.052 μm/pixel for revealing the elemental deposition patterns. Image processing to create elemental maps involved 2 × 2 pixel binning and

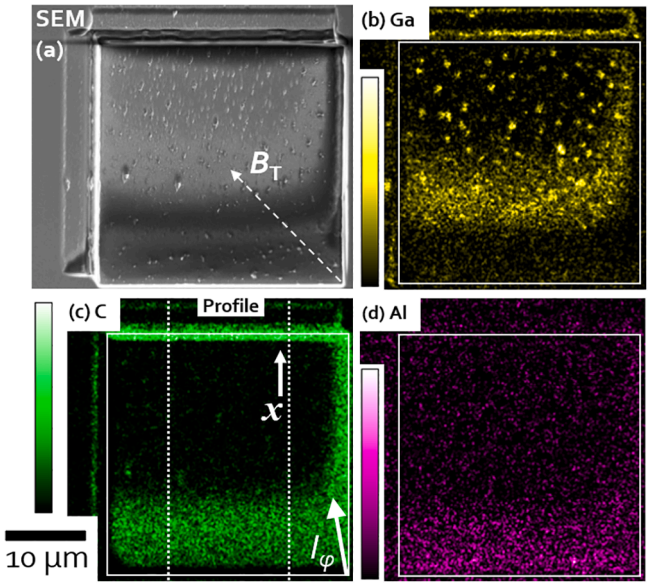

Fig. 5. (a) Top view SEM image and EDS maps of (b) Ga, (c) C, and (d) Al for the **T31** trench. The background intensity for the EDS maps was subtracted using the method described in Section 4.1. The color scales on the left correspond to the range from zero to the maximum intensity for each map (see online version for color). In (c), we annotate the *x*-direction that specifies the profile direction used to determine the polar IAD, and the area outlined by dashed lines indicates the area used to derive the *x*-direction intensity profiles in Fig. 6. The peak azimuthal incident ion direction I_φ ($\varphi = -35°$, Section 3) is also shown in (c).

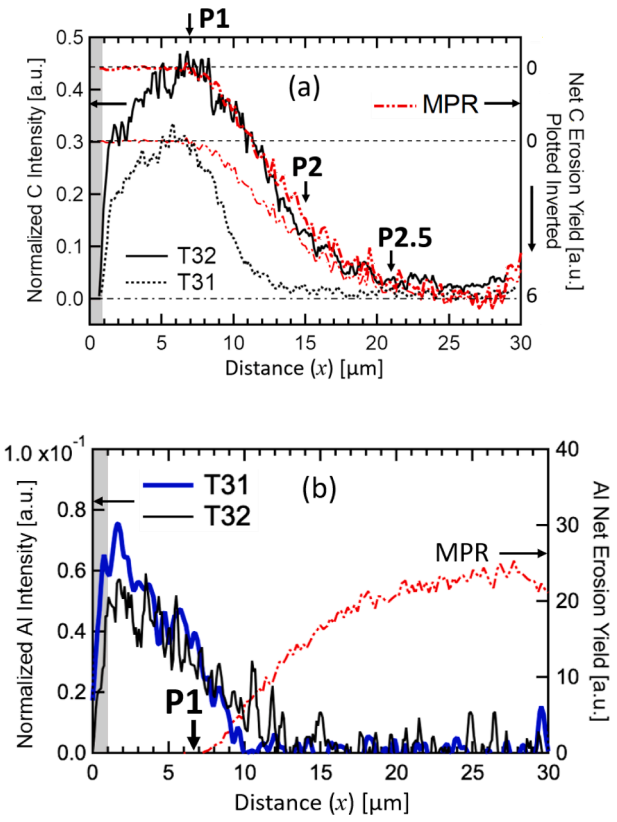

Fig. 6. (a) Net erosion yield profile for D ions incident on C calculated by MPR for a 3-μm deep trench, and the C intensity profile measured by EDS for 3-μm deep trenches **T31** and **T32**. Red dashed lines represent the MPR profile inverted and scaled to the same peak height as the **T31** and **T32** C intensity profiles, respectively. (b) Net erosion yield profile for D ions incident on Al as calculated by MPR for a 3-μm deep trench, and Al intensity profiles measured by EDS for trenches **T31** and **T32**. The same arbitrary units are used for both the **T31** and **T32** data in both plots. The region $x < 1$ μm is masked because X-rays from that area are not detectable during EDS analysis (Section 4.1).

then 3 × 3 pixel Kernel imaging processing (Box Blur normalization). The average EDS intensity from location **3** in Fig. 3 consisted mainly of bremsstrahlung continuum emission and was subtracted from the original intensity mappings as a background signal. Fig. 5 shows elemental maps of the dominant redeposited C and Al materials in the ion-shadowed region for the **T31** trench. Fig. 5(c) shows that sputtered C that was redeposited on the trench floor remained in the area at the bottom of the image that was shadowed from the incident D ions. Here again the deposition pattern is consistent with I_φ, as seen in the SEM image in Fig. 3. C is the primary background impurity in DIII-D plasmas, and the DiMES sample holder is also made of graphite. The 1-μm wide dark region seen at the bottom of Fig. 5(c), just next to the ion upstream wall, arises because X-rays from that region are blocked by the wall from reaching the detector location. We confirmed that the dark region was made due to the EDS alignment by rotating the sample. Hence, the data in this area will not be used for analysis. A similar spatial distribution is apparent in Fig. 5(d) for redeposited Al that was originally eroded from the 100-μm thick Al coating on the sample. In a previous experiment that exposed a partially Al-coated DiMES sample [22], a 2D optical imaging of neutral Al emission (Fig. 4 of ref. [22]) confirmed that Al originated from the Al-coated area, not as a residual impurity in the vessel. The elemental maps of O (not shown) were similar to the C deposition patterns because O originates mostly from oxidized carbon contamination and oxidized aluminum due to ambient air exposure. The Ga EDS map in Fig. 5(b) confirms that the microparticles seen in the SEM images in Figs. 3 and 5(a) are Ga clusters.

In some cases, the IAD can be seen in the net deposition profile in the trench. There are two conditions for this. First the gross deposition in the trench should be close to uniform. The Al coating on the samples and DiMES graphite holder are mm^2 – cm^2 in area, and thus the C and Al ion flux from those areas onto the general area of the 30 × 30 μm trench should be uniform. Monte Carlo impurity migration models such as REDEP/WBC [23–25], ERO [26], and GITR [27,28] have traced the trajectory of prompt redeposition materials on the divertor. REDEP/WBC modeling [24] reported that the ion impact angle of re-deposited particles for typical tokamak divertor plasmas are ~45° for light species (Be, C) and ~20–30° for heavy species (Mo, W). These values are much steeper than the predicted main D ion impact angle ($\theta > 68°$ in Fig. 4), so the area at the bottom of the trench floor that is shadowed by the trench walls is small. Hence, we assume that the redeposited-ion flux on the trench floor is close to uniform in the area irradiated by the main D ion flux. Also, preliminary results from a later experiment with a 4-μm deep trench (rotated clockwise by 45° from **T31** and **T32**) show a C deposition that is uniform to ±5% in the shadowed area from 2 to 7 μm from the wall. This data will be reported in a subsequent publication. A second condition for the net deposition to reveal the IAD is that the gross erosion and gross deposition be somewhat balanced. If the deposition is too low then it can be wholly eroded together with the information on the IAD. Fortunately, there was one case (Fig. 6(a) **T32**) where the deposition was sufficient to reveal the IAD.

The line profile analysis will be performed in the following sections using those EDS deposition maps along the *x*-direction shown in Fig. 5 (c). The calculated peak azimuthal incident ion direction I_φ (Fig. 5(c)) is oriented to $\varphi = -35°$, which is $\Delta\varphi = +10°$ of the *x*-direction ($\varphi = -45°$). Because cos10° ~1, the peak azimuthal incident ion direction has a negligible effect on the geometric calculation on the line profile along the *x*-direction. Hence, the line profile in the *x*-direction will be used to reveal the contribution from the polar (θ) IAD on the deposition pattern.

4.2. Comparison of the net deposition profiles of C and Al to MPR code predictions

The EDS maps for the **T31** (Fig. 5) and **T32** trenches were integrated over a 15-μm wide area, as illustrated by the dashed lines in Fig. 5(c), and plotted versus the distance (x) from the upstream wall in Fig. 6(a) for C and Fig. 6(b) for Al. Both C and Al profiles are normalized to the intensity of Si at the outer trench area where the Si surface is barely covered by impurities (as confirmed by the EDS spectrum (not shown) obtained at location **3** in Fig. 3). We see in Fig. 6(a) that the peak intensity of C for **T32** is higher than **T31**. Indeed, **T32** is located only 0.5 mm away from the graphite DiMES head boundary (Fig. 1(b)) while **T31** is 2 mm away. This indicates that the DiMES holder is a dominant source of C deposition on the samples. In contrast, the peak intensity of Al for **T31** is higher than **T32** in Fig. 6(b), which is consistent with the **T31** trench location at 1 mm from the Al boundary (Fig. 1(b)), while **T32** is located at 2.5 mm. This trend matches the Al redeposition mapping measured in previous experiments [22]. Fig. 6(a) and (b) also include the net erosion yield of C and Al as calculated by the MPR code for each trench. In Fig. 6(a), the MPR C net erosion profile was *inverted* to aid comparison to the C intensity profile.

These MPR profiles in Fig. 6(a) and (b) predict ion erosion everywhere except for the 7-μm wide area of the trench floor that is shadowed from the incident ions. Although the MPR calculation used the sputtering angular dependence of Si instead of that for Al (as described in Section 3), the shadowing region is only affected by the **P1** of the polar (θ) D IAD. The shadowed width can also be estimated by a geometric calculation, e.g., $w_{\mathbf{P1}} = \tan(\mathbf{P1} = 68^{\circ}) \times 3\ \mu\text{m} \approx 7\ \mu\text{m}$. The shadowed width is also depicted in Fig. 2 with the trench cross section profile. We note that the MPR calculation also uses the azimuthal IAD as input (Section 3). The **T32** and **T31** EDS profile of C in Fig. 6(a) shows rollover around 6–7 μm (**P1**) indicating that there is sputtering by D ions beyond this location (edge of the shadowed area). The EDS profiles in Fig. 6(b) show Al intensity at 0–10 μm from the ion upstream wall for **T31** and at 0–11 μm for **T32**. These Al intensities are in good agreement with the MPR predictions of ion erosion and thus the shadowed areas for these cases. The redeposition behavior of C and Al impurities in the shadowed region, x = 1–7 μm, will be a topic of a future publication.

In Fig. 6(a) the **T32** MPR and EDS profiles for C show remarkably good agreement over the non-shadowed range at 7–30 μm from the wall. Such a comparison beyond the shadowed area cannot be made for the Al profiles of **T31** nor **T32** in Fig. 6(b) because the Al remained only in the area $x < 10$ μm. The EDS intensity analysis in the shadowed floor (location **1** in Fig. 3), using coefficients provided in the AZtec software, showed that the redeposited amount of Al was 1/6 of that of C while the sputtering yields of Al and C show similar values of 0.04 atoms/ion for Al and 0.02 atoms/ion for C when E_{impact} = 150–200 eV [2]. This indicates that the thinner Al deposits were completely sputtered away by the ions incident for $x \geq 10$ μm (Fig. 6(b)). The same reasoning can also be applied to C for **T31**. The sputtering rate could exceed the redeposition rate of C at 13–30 μm from the wall, and hence the deposition profile does not follow the MPR net erosion profile in this region. On the other hand, good agreement between the C deposition profile and that calculated from MPR was observed in x = 7–20 μm for **T32**, which is much closer to the graphite DiMES head than **T31**. This indicates that there was a balance between the C redeposition and sputtering rates that reveals the characteristics of the erosion profile in this range. Thus, the comparison of the C EDS profile of **T32** with the C MPR net erosion profile provides a verification of the predicted IADs.

The sputtering rate at a given location on the trench floor depends on the product of the flux at a particular angle and sputtering coefficient at this angle, integrated over the range of angles that can reach that point on the floor. The sputtering yield for C at a specific polar angle was multiplied by the corresponding ion fraction at that angle (Section 3), and is plotted in Fig. 4 as the "effective sputtering yield". Beyond the shadowed range, the trench floor is subject to ion flux with incident polar angles in a range from $\theta = 68^{\circ}$(**P1**) to a "cutoff angle" determined by the distance to the trench upstream wall and its height. Ions incident at a polar incident angle above the cutoff angle will be shadowed by the wall. The effective sputtering yield peaks around the polar angle θ = 77-79°(**P2**) (Fig. 4). So, the integration over incident ion angle will have an inflection point at this angle. The location $w_{\mathbf{P2}} = \tan(\theta = 79^{\circ}) \times 3\ \mu\text{m} \approx 15\ \mu\text{m}$ (**P2**) corresponds to the location that has the cutoff angle $\theta = 79^{\circ}$. We see an inflection in the MPR net erosion at 15 μm (**P2**) in Fig. 6, and it is also seen in the EDS C deposition profile for **T32**. The location $w_{\mathbf{P2.5}} = \tan(\theta = 82^{\circ}) \times 3\mu\text{m} \approx 21\mu\text{m}$ (labeled '**P2.5**') has a cutoff angle $\theta = 82^{\circ}$. The effective sputtering yield of C becomes one-half of the peak when $\theta = 82^{\circ}$ (labeled '**P2.5**' in Fig. 4). The integrated value of the effective sputtering yield for $\theta = 82^{\circ}$ is ~90% of the maximum integrated value for the entire angle range up to 90°. This is consistent with the nearly flat MPR profile for x = 20–30 μm in Fig. 6(a). Such good general agreement for the **T32** profile supports the inputted polar IAD.

5. Summary

A Si(1 1 1) disc sample with specially designed micro-trenches was exposed to DIII-D L-mode discharges to reveal the impact angle distribution of D ions in the DIII-D divertor. Aluminum that was deposited on one-half of the surface of the disc was eroded and redeposited on the trench floors during plasma exposures, together with C eroded from the DiMES head and the vessel. Post-exposure SEM imaging showed impurity materials remained at the portion of the floor of the trench that was shadowed from the incident ions by the walls. Polar and azimuthal IADs were previously predicted for this discharge configuration by a non-collisional kinetic model that used an analytically calculated Chodura sheath potential [3]. These IADs were input to the MPR code to give the net erosion profiles of C and Al exposed to D ion flux on the trenches. The areal C and Al intensities were measured by EDS and compared with the MPR calculations. The comparison shows good agreement of the deposition profile of C and the polar IAD. The characteristic structure of predicted polar IAD in the range up to 83.5° was verified by the C net deposition profile. These results are the first reported experimental evidence verifying the structure of the computationally predicted polar IAD. These agreements also support the assumptions of the Chodura sheath modeling used in the IAD calculations.

CRediT authorship contribution statement

S. Abe: Conceptualization, Methodology, Software, Validation, Formal analysis, Investigation, Data curation, Writing - original draft, Visualization. **C.H. Skinner:** Conceptualization, Methodology, Supervision, Project administration, Funding acquisition. **I. Bykov:** Investigation, Resources, Data curation. **Y.W. Yeh:** Resources. **A. Lasa:** Methodology, Software. **J. Coburn:** Methodology, Software. **D.L. Rudakov:** Investigation, Resources, Data curation. **C.J. Lasnier:** Resources, Data curation. **H.Q. Wang:** Resources, Data curation. **A.G. McLean:** Resources, Data curation. **T. Abrams:** Project administration, Funding acquisition. **B.E. Koel:** Supervision, Project administration, Funding acquisition.

Declaration of Competing Interest

The authors declare that they have no known competing financial interests or personal relationships that could have appeared to influence the work reported in this paper.

Acknowledgements

The authors thank Roman Akhmechet, Zuzanna A. Lewicka, and David S. Barth of PRISM (Princeton University) for fabricating the aluminum coating, and John J. Schreiber for SEM/EDS analysis. We

thank Dean Buchenauer and Josh Whaley (Sandia National Laboratories) for providing the Si(111) sample discs. We also thank Christopher P. Chrobak for advice on his IAD prediction. BEK acknowledges support of this work by the U.S. Department of Energy, Office of Science/Fusion Energy Sciences under Award Number DE-SC0019308. This work is also supported by US DOE Contract Nos. DE-AC02-09CH11466 and DE-FC02-04ER54698. The authors acknowledge the use of Princeton's Imaging and Analysis Center, which is partially supported through the Princeton Center for Complex Materials (PCCM), a National Science Foundation (NSF)-MRSEC program (DMR-2011750).

References

[1] W. Eckstein, C. Garcia-Rosales, J. Roth, and W. Otternberger, Sputtering Data, IPP 9/82 February (1993).
[2] R. Behrisch, W. Eckstein, Sputtering Particle Bombard. (2007).
[3] C.P. Chrobak, et al., Nucl. Fusion 58 (2018), 106019.
[4] P.C. Stangeby, Nucl. Fusion 52 (2012), 083012.
[5] D. Coulette, G. Manfredi, Plasma Phys. Control. Fusion 58 (2016), 025008.
[6] K. Schmid, et al., Nucl. Fusion 50 (2010), 105004.
[7] R. Khaziev, D. Curreli, Phys. Plasmas 22 (2015), 043503.
[8] C.H. Skinner, C.P. Chrobak, M.A. Jaworski, R. Kaita, B.E. Koel, Nucl. Mater. Energy 18 (2019) 35–40.
[9] J. Coburn, et al., Nucl. Mater. Energy 19 (2019) 316–323.
[10] D.L. Rudakov, et al., Nucl. Fusion 49 (2009), 085022.
[11] I. Borodkina, et al., Contrib. Plasma Phys 56 (6–8) (2016) 640–645.
[12] I. Bykov et al., Nucl. Fusion, under review (2021).
[13] J. Watkins, D. Taussig, R. Boivin, R.E. Nygren, Rev. Sci. Instrum. 79 (2008) 10F125.
[14] A. Lasa and J. Coburn, "MPR" source code, https://github.com/ORNL-Fusion/MPR.
[15] A. Lasa, et al., Abstract ID: BAPS.2016.DPP.TP10.88, APS-DPP, San Jose, CA, (2016). http://meetings.aps.org/link/BAPS.2016.DPP.TP10.88.
[16] P.C. Stangeby, The Plasma Boundary of Magnetic Fusion Devices, IOP Publishing, Bristol, 2000.
[17] W. Eckstein, 'Reflection (Backscattering)', IPP 17/12 August (2009).
[18] E. Oyarzabal, R.P. Doerner, M. Shimada, G.R. Tynan, J. Appl. Phys. 104 (2008), 043305.
[19] J. Roth, J. Nucl. Mater. 266–269 (1999) 51.
[20] M. Balden, J. Roth, J. Nucl. Mater. 351–355 (2000) 279.
[21] L. Zarraoa, et al., Sci. Rep. 9 (2019) 16263.
[22] C.P. Chrobak, et al., Nucl. Mater. Energy 12 (2017) 441–446.
[23] J.N. Brooks, D.G. Whyte, Nucl. Fusion 39 (1999) 525.
[24] J.N. Brooks, Fusion Eng. Des. 60 (2002) 515.
[25] J.N. Brooks, J.D. Elder, A.G. McLean, D.L. Rudakov, P.C. Stangeby, W.R. Wampler, Fus. Eng. Des. 94 (2015) 67–71.
[26] A. Kirschner, V. Philipps, J. Winter, U. Kögler, Nucl. Fusion 40 (2000) 989–1001.
[27] A. Lasa, et al., Phys. Scr. (2020), 014041.
[28] T.R. Younkin, et al., Comput. Phys. Commun. (2021), 107885.